

Energy & Environmental Science

Accepted Manuscript



This is an *Accepted Manuscript*, which has been through the Royal Society of Chemistry peer review process and has been accepted for publication.

Accepted Manuscripts are published online shortly after acceptance, before technical editing, formatting and proof reading. Using this free service, authors can make their results available to the community, in citable form, before we publish the edited article. We will replace this *Accepted Manuscript* with the edited and formatted *Advance Article* as soon as it is available.

You can find more information about *Accepted Manuscripts* in the [Information for Authors](#).

Please note that technical editing may introduce minor changes to the text and/or graphics, which may alter content. The journal's standard [Terms & Conditions](#) and the [Ethical guidelines](#) still apply. In no event shall the Royal Society of Chemistry be held responsible for any errors or omissions in this *Accepted Manuscript* or any consequences arising from the use of any information it contains.

A long-life lithium-ion battery with highly porous TiNb₂O₇ anode for large-scale electrical energy storage

Cite this: DOI: 10.1039/x0xx00000x

Bingkun Guo^{a†}, Xiqian Yu^{b†}, Xiaoguang Sun^a, Miaofang Chi^c, Zhen-An Qiao^a, Jue Liu^b,
Yong-Sheng Hu^{d*}, Xiao-Qing Yang^b, John B. Goodenough^e, Sheng Dai^{a,f*}

Received 00th January 2012,
Accepted 00th January 2012

DOI: 10.1039/x0xx00000x

www.rsc.org/

High performance TiNb₂O₇ anode material with nanoporous nature which was prepared by a facile approach, exhibits an average storage voltage of 1.66 V, a reversible capacity of 281 mAh g⁻¹, and 84% capacity retention after 1000 cycles, suitable for long-life stationary lithium-ion batteries.

Large-scale electrical-energy storage with long-life, high efficiency, high safety and low cost is a key technology for the development of smart grid and renewable energy sources, including solar and wind powers. Electrical energy is most conveniently stored in a rechargeable battery. Lithium-ion batteries (LIBs) represent one of the most important and advanced technologies among rechargeable batteries owing to their high energy density and low environmental impact¹⁻⁶. However, LIBs using graphite as anode material^{7, 8} cannot meet the stringent requirements for these applications because formation of a passivating solid-electrolyte interphase (SEI) layer on graphitic carbon^{2, 9} robs lithium irreversibly from the cathode on the initial charge and the charging rate is limited because of plating of lithium on the SEI layer at the voltage required for a fast charge. Therefore, it would be advantageous to have a high capacity anode with its Fermi energy E_F below the lowest unoccupied molecular orbital (LUMO) of the electrolytes so as to avoid formation of an anode SEI layer. The standard organic Li⁺ liquid-carbonate electrolytes have a LUMO near 1.2 eV versus Li⁺/Li, and an anode E_F at 1.5 eV below that of lithium may compensate the loss of cell voltage by increasing the cathode capacity, by providing safe high-rate performance, and by providing a longer cell cycle and shelf life. The leading candidate has been Li₄Ti₅O₁₂ (LTO) with an E_F 1.55 eV below that of lithium as it shows the expected excellent cycle life and rate capability.¹⁰⁻¹⁵ However, the low storage capacity of LTO (~160 mAh g⁻¹) has limited its further application.

Recently, TiNb₂O₇ has been proposed by Han *et al.* as a high-capacity anode material and shows great promise to replace LTO

anode.^{16, 17} The theoretical capacity of TiNb₂O₇ is 387 mAh g⁻¹. Practically, a reversible capacity of around 280 mAh g⁻¹ has been obtained in a voltage range of 1.0-2.5 V,¹⁶ which is almost two times higher than that of LTO (~160 mAh g⁻¹) with similar average storage voltage. Unfortunately, an intrinsic low electronic and ionic conductivity have restricted its electrochemical performances. The electronic conductivity of materials can be effectively improved by doping or carbon coating.^{13, 16} The characteristic diffusion time for lithium diffusion in electrode materials is $\tau \sim L^2/D$, where L is the diffusion length and D is the diffusion coefficient for Li⁺ ion in the solid.¹⁸⁻²⁰ Therefore, reducing the particle size can dramatically reduce the Li⁺ ion diffusion time and improve the Li insertion/extraction kinetics because of the shorter Li⁺ solid diffusion pathway. This approach has inspired many researchers on developing nano-sized materials such as nanowires,^{21, 22} nanotubes^{23, 24}, and nanoparticles,^{25, 26} for high rate capability electrodes. Even though attractive electrochemical performance has been achieved, some disadvantages such as low volumetric energy density, the weak adhesion of nano-sized materials to the current collector, and most importantly, health hazards, have hindered their practical applications in LIBs.²⁷⁻²⁹

Here, we report a simple, large-scale sol-gel method for synthesis of nanoporous titanium-niobium oxides.^{30, 31} Unlike nano-sized materials, nanoporous materials with micrometer-sized particles can not only provide porous channels for rapid access of Li⁺ ions into the particle bulk to decrease the Li⁺ diffusion length, but also can improve handling to avoid inhalation hazards and offer high packing density.^{29, 32, 33} In a typical synthesis, niobium ethoxide (Nb(OC₂H₅)₅) and tetrabutylorthotitanate (Ti(OC₄H₉)₄) were used as precursors and commercial Block-copolymer F127 was used as surfactant. The final material was thermally treated at different temperatures (400°C, 600°C, 700°C, 850°C, 1000°C) in air, as described in detail in the experimental part. Figure 1a provides a schematic diagram of the formation mechanism for nanoporous TiNb₂O₇.

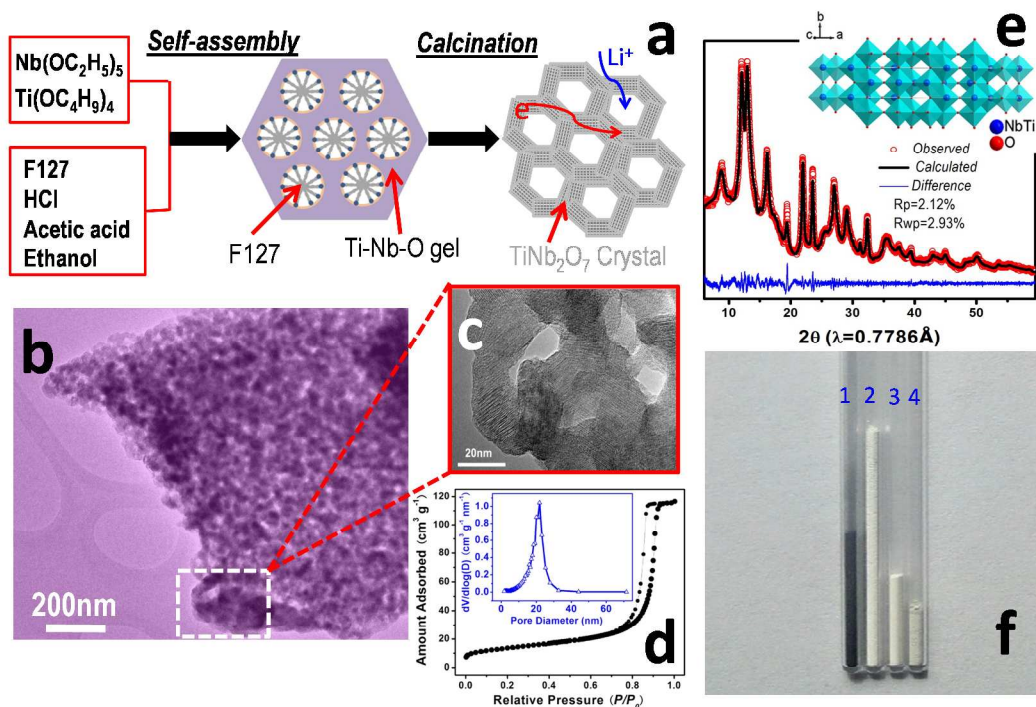


Figure 1 Porous structure characterizations. a, Schematic diagram of the formation mechanism for nanoporous TiNb_2O_7 . b, TEM image of TNO-700. c, HR-TEM image of TNO-700. d, Nitrogen adsorption-desorption isotherm and corresponding pore size distribution curve (Inset) for TNO-700. e, Observed and simulated XRD patterns of TNO-700 with Rietveld refinement; inset figure: crystal structure view of TiNb_2O_7 , lattice parameters in $C2/m$ space group, $a = 20.386$ (14) Å, $b = 3.802$ (4) Å, $c = 11.902$ (12) Å, $\alpha = \gamma = 90^\circ$, $\beta = 120.369$ (48). f, Volume occupied comparison of (1) commercial graphite (2) commercial $\text{Li}_4\text{Ti}_5\text{O}_{12}$ nanopowder (50 nm) (3) microporous $\text{Li}_4\text{Ti}_5\text{O}_{12}$ ¹⁰ and (4) TNO-700 samples with the same mass.

Figure S1 shows the nitrogen adsorption-desorption isotherms and corresponding pore size distribution curves for the titanium-niobium oxides thermally treated at different temperatures (400°C, 600°C, 700°C, 850°C, 1000°C). As shown in this figure, the sample obtained at 400°C (TNO-400) features a highly mesoporous morphology with a uniform pore size of 5.6 nm; the pores are formed by pyrolysis of block-copolymer F127 micelles. The sample starts to crystallize at 600°C (Figure S2) and bimodal pore size distribution can be observed. The larger pores at the TNO-600 sample could be attributed to the TiNb_2O_7 nanocrystal growth accompanied by the collapse of primary mesoporosity. After treatment at 700°C, the sample is highly crystalline (Figure S2) and, all the pores for TNO-700 should be interparticle pores (around 20 nm). Meanwhile, as the calcination temperature increases, the BET surface areas of samples decrease from 85 to 48 $\text{m}^2 \text{g}^{-1}$. Furthermore, nanoporous TiNb_2O_7 shows non-porous characteristics after heating to 1000 °C. The SEM and TEM results also show the same evolution process. As shown in Figure 1b and 1c, TNO-700 is highly porous in nature with 20-30 nm pore size and primary particle size. The sample is fully crystalline and composed of nanocrystals interconnected into a porous scaffold. The preparation at the higher temperature of 850 °C results in an increase in particle size (50-100 nm) and pore size (40-60 nm) (Figure S3). As expected, TNO-1000 sample collapses to bulk particles and shows non-porous characteristics (Figure S3).

The crystal structure of TiNb_2O_7 is illustrated in Figure 1e; each metal atom (Ti and Nb) is coordinated with six oxygen atoms

forming an octahedral group. These octahedra are connected through corner and edge sharing to form a crystallographic-shear framework structure. The XRD patterns of the as-prepared TiNb_2O_7 samples at various temperatures are shown in Figure S2. All peaks for TNO-700 and TNO-850 reveal a broad feature, indicative of a nano-sized primary particle, as is also observed from SEM and TEM results (Figure 1c and Figure S3). The patterns yield the best matching to a monoclinic crystallographic system with all of the diffraction peaks in good agreement with the JCPDS No. 77-1374. No separate phases of TiO_2 and Nb_2O_5 were found, suggesting a phase-pure TiNb_2O_7 can be obtained at 700°C for around 3 h, which can greatly reduce production cost as compared to the conventional solid-state approach required above 1000°C and around 24 h (Figure S4).^{16, 34, 35} The Rietveld refinement within a space group of monoclinic $C2/m$ gives the lattice parameters $a = 20.386$ (14) Å, $b = 3.802$ (4) Å, $c = 11.902$ (12) Å, $\alpha = \gamma = 90^\circ$, $\beta = 120.369$ (48), which is close to the experimental data of the micro-sized material.¹⁶

Figure 1f illustrates the volume occupied by the same mass of commercial graphite, commercial $\text{Li}_4\text{Ti}_5\text{O}_{12}$ nanopowder (50 nm), microporous $\text{Li}_4\text{Ti}_5\text{O}_{12}$ ¹⁰, and TNO-700 samples. Although the nanoporous TNO-700 has a surface area of 45 $\text{m}^2 \text{g}^{-1}$, it still possesses high packing density. As shown in Figure 1f, the packing density of nanoporous TNO-700 is not only much higher than microporous $\text{Li}_4\text{Ti}_5\text{O}_{12}$, but also almost 4 times higher than that of commercial graphite, indicating nano porous TNO-700 has much higher volumetric storage capacity than both nanostructure $\text{Li}_4\text{Ti}_5\text{O}_{12}$

and graphite, which is a desirable property for a space-limited application.

Coin cells (2032) with Li foil as counter electrode were used to evaluate the electrochemical performance of the as-synthesized materials. All cells were cycled between 1.0 V and 3.0 V. Figure 2a shows the galvanostatic discharge (Li insertion)/charge (Li extraction) profiles for the TNO-700 anode at a low current rate of 0.1C (38.7 mA g⁻¹). The reversible capacity of TNO-700 is 281 mAh g⁻¹, which is almost two times higher than that of LTO (~160 mAh g⁻¹) and also comparable to that of commercial graphite (300-330 mAh g⁻¹). Besides capacity and safety, another key parameter for commercial application of the anode material is coulombic efficiency, as the lithium supplied by the lithiated cathode materials is limited in the full cell. As shown in Figure S6, the initial coulombic efficiency of the TNO-700 electrode is as high as 97% at 1C, much higher than previously reported results about TiNb₂O₇-base materials (80-85%)^{16, 34, 35} and even higher than that of commercial graphite electrode (around 90%).^{7, 8} After a few cycles at 1C, the coulombic efficiency quickly increases to 100% and is maintained even after 380 cycles. As a comparison, the coulombic efficiency of previously reported TiNb₂O₇ is only around 97%,^{16, 34,}

step³⁵ (Supplementary Table S2). For practical applications (in full-cell configuration), high current delivery on demand (high power), which is the charge process (Li extraction) for anode materials in a half-cell, is very important. As a demonstration for such capability, Figure 2c displays the charge rate performance of the nanoporous TNO-700 with the discharge rate fixed at 1C. As shown in the figure an extremely high charging rate can be achieved with the nanoporous TNO-700. For example, there is even no capacity loss observed from 1C to 20C; 206 mAh g⁻¹ can be achieved at 50C (19.4 A g⁻¹, 72s full charge), two times higher than previously reported^{13, 35}. Even at a charging rate of 100C (38.7 A g⁻¹, 36s full charge), 160 mAh g⁻¹ can still be obtained, which is close to the theoretical capacity of a LTO anode (170 mAh g⁻¹). To the best of our knowledge, this is the best rate performance for titanium-based oxides so far. Besides excellent rate capability, the nanoporous TNO-700 also has superior capacity retention at high rates. Figure 2d presents data showing that the capacity of the nanoporous TNO-700 is stabilized at 200 mAh g⁻¹ even after 1000 cycles at 5C with a capacity retention of 84%; and more impressively, the coulombic efficiency is always stabilized at 100% after the first few cycles.

The Li-storage properties of TiNb₂O₇ samples prepared at 850 °C

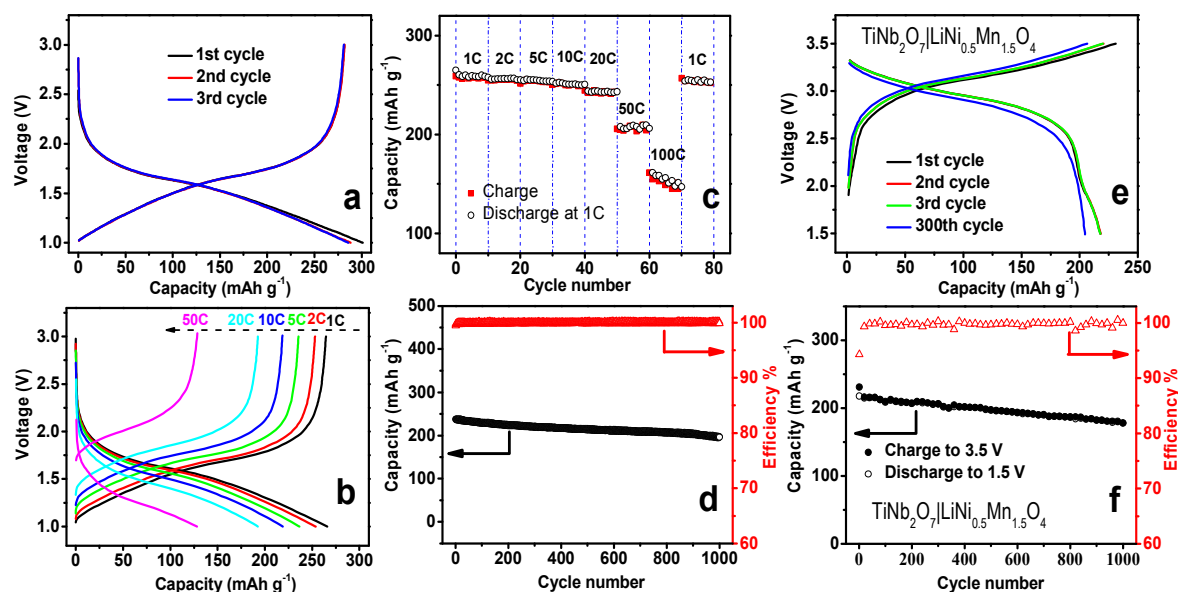


Figure 2 Li storage performance of nanoporous TiNb₂O₇. a, Typical discharge/charge curves of the TNO-700 anode at a current rate of 0.1C. b, Discharge/charge curves of the TNO-700 anode at different current rates. c, Capacity retention of the TNO-700 anode at various rates: discharge current rate fixed at 1C. d, Cyclic performance of the TNO-700 anode at a current rate of 5C after aging at 0.1 C for 5 cycles. e and f, Typical discharge/charge curves and cyclic performance for the LNMO-TNO full cell at 1C with capacity limited by TNO cycled between 1.5 and 3.5 V (after aging at 0.1C for 5 cycles).

³⁵ which will lose 95% of its capacity after 100 cycles ($0.97^{100}=0.047$) in the full cell.

Figure 2b shows the rate performance of the nanoporous TNO-700. It can be seen that the specific capacities of the TNO-700 are as high as 236 mAh g⁻¹ at 5C (1.94 A g⁻¹), 219 mAh g⁻¹ at 10C (3.87 A g⁻¹) and 195 mAh g⁻¹ at 20C (7.74 A g⁻¹). Even at a high rate of 50C (19.4 A g⁻¹), the specific capacity is as high as 128 mAh g⁻¹, which is comparable to the capacity of LTO (130 mAh g⁻¹) at a much lower rate of 10C.¹⁰ The rate performance of nanoporous TNO-700 is much better than that of bulk, carbon-coated, doped, other nanostructured TiNb₂O₇ samples and commercial graphite materials^{16, 35, 36}. TNO has an asymmetric charge/discharge process with the discharge process (Li insertion) being the rate-limiting

(TNO-850) and at 1000 °C (TNO-1000) were also evaluated under identical conditions (Figure S7). The TNO-850 shows similar Li storage behavior as TNO-700, such as high capacity (286 mAh g⁻¹ at 0.1C), excellent rate performance and high coulombic efficiency. However, the TNO-850 suffers from capacity fading with cycling, with a capacity loss of 40% after 600 cycles at 5C. In contrast to TNO-700 and TNO-850, the non-porous TNO-1000 shows much poorer electrochemical properties (Figure S7). The capacity of TNO-1000 is about 250 mAh g⁻¹ at a low rate of 1C, close to that of porous materials and previously reported results.¹⁶ However, a large capacity loss is observed when the current rate is increased from 1C to 50C. For example, 120 mAh g⁻¹ and 40 mAh g⁻¹ are obtained at 10C and 50C, respectively, only half that of the nanoporous TNO-

700 at the same rates (219 mAh g⁻¹ at 10C, 128 mAh g⁻¹ at 50C). Furthermore, the TNO-1000 also suffers from serious capacity fading with a capacity loss of 50% after 600 cycles at 5C. Clearly, the high rate capability, excellent cyclic stability and high coulombic efficiency observed for the nanoporous TNO-700 can be ascribed to the interconnected nanoporous framework composed of nanocrystals having a variety of favorable properties as mentioned above. First, the interconnected channels make facile diffusion of the liquid electrolyte into the bulk of the electrode material and greatly reduce the solid-state diffusion length for Li (Figure 1a). Second, the high value ($\sim 10^{-12}$ cm² s⁻¹, Table S2) of the Li⁺ diffusion coefficient in TNO-700, which is similar to Li diffusion in LiCoO₂ and LiMn₂O₄, significantly improves the intrinsic kinetic property and enables the superior rate capability. Third, nanoporous TNO provides a continuous electronic conduction path along well-connected nanocrystals (note that a small amount of Li insertion into TNO will significantly increase the electronic conductivity of TNO).³⁴ (Figure 1a). Finally, these interconnected channels can alleviate lattice stress/strain generated from the volume expansion and contraction associated with lithium insertion and extraction, thus improving the cycling stability and coulombic efficiency of electrodes. The above favorable properties clearly show that nanoporous TNO-700 is a very promising candidate for practical applications in lithium ion batteries.

As proposed by Han and Goodenough,¹⁷ the TNO anode can combine with the LiNi_{0.5}Mn_{1.5}O₄ (LNMO) cathode to assemble a 3-V full cell. Based on a stable capacity delivery of 280 mAh g⁻¹ and

125 mAh g⁻¹ for a TNO anode and LNMO cathode respectively, a maximum energy density of 250 Wh kg⁻¹ (based on the total weight of anode and cathode materials) can be obtained for the 3 V system. In virtue of the high packing density of the electrode materials, our TNO-LNMO full cell is also expected to have a high volumetric energy density. Figure 2e shows typical discharge/charge curves for the TNO-LNMO full cell at 1C with capacity limited by the TNO anode. As expected from their respective voltages, the full cell gives rise to an operating voltage around 3.0 V. The reversible capacity of the 3-V full cell at 1C is 220 mAh g⁻¹. Furthermore, the full cell displays excellent cycle stability, with a capacity retention of 82% even after 1000 cycles (Figure 2f). To our knowledge, our TNO-LNMO battery outperforms other competitor systems for operation of a large-scale stationary energy storage.

To further understand the structural changes of TNO during Li insertion and extraction, an *in situ* XRD experiment was performed; the results are given in Figure 3a. The structural changes could be divided into three regions: two solid-solution and one 2-phase coexistence regions. The first solid-solution reaction (SS1) occurs during the initial discharge before scan 4 (labeled as S4), corresponding to Li₀TiNb₂O₇ to Li₁TiNb₂O₇ and the second solid solution reaction (SS2) takes place during the final stage of discharge from scan 7 to scan 15, corresponding to Li_{1.75}TiNb₂O₇ and Li_{3.6}TiNb₂O₇. (From scan 4 to scan 7, a 2-phase co-existence region was observed through the significant peak broadening.) The solid-solution nature of these two regions is evidenced by the continuous peak shifting and their structures were identified as

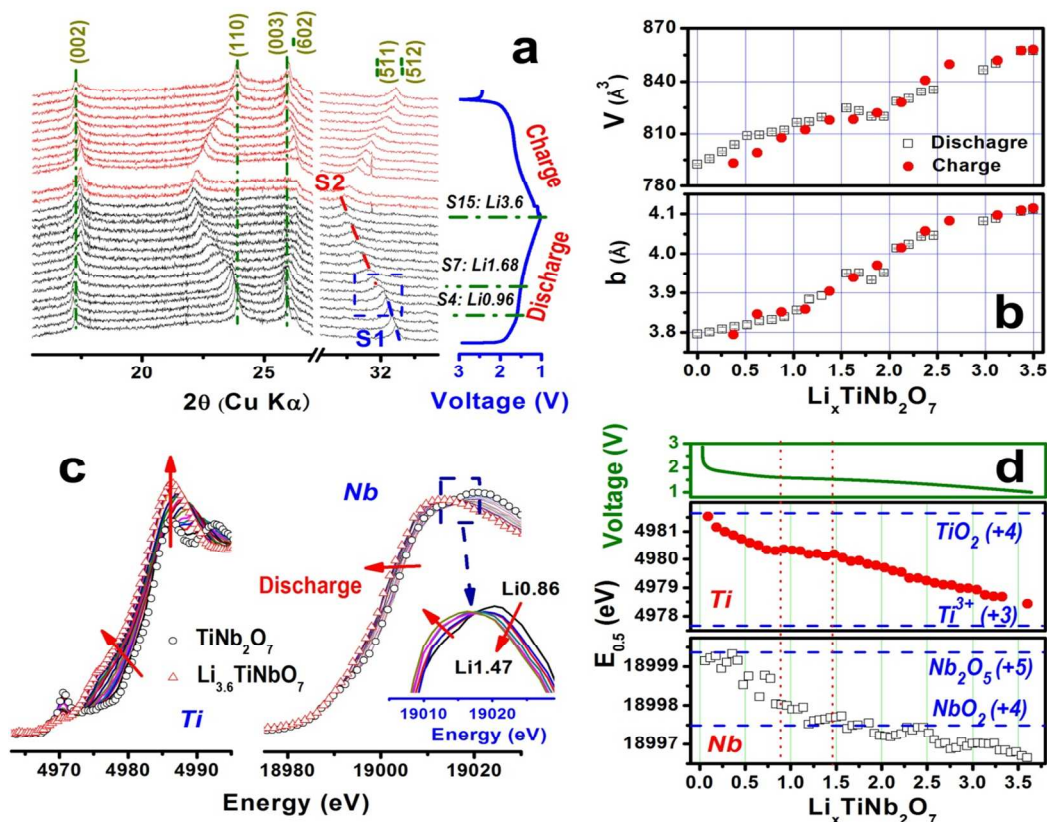


Figure 3 Structure changes of $\text{Li}_x\text{TiNb}_2\text{O}_7$ during Li insertion/extraction. **a**, *In situ* XRD patterns collected during initial discharge and charge at a constant current rate of C/8 between 1.0V and 3.0 V. **b**, The unit cell volume "V" and lattice parameter "b" calculated from "Label fitting" as a function of "x" in $\text{Li}_x\text{TiNb}_2\text{O}_7$ ("x" derived from the capacity obtained; open circle: during discharge; solid dot: during charge). **c**, *In situ* Ti K-edge and Nb K-edge XANES spectra collected during initial discharge at C/10 rate between 1.0V and 3.0 V voltage range (inset Figure: isosbestic point on spectra between $x=0.86$ and $x=1.47$ indicates a two-phase reaction region). **d**, Valence state variation of Ti and Nb during initial discharge estimated from the Ti and Nb XANES edge positions.

monoclinic phases with the same $C2/m$ space group, but different lattice parameters. The discharge curve shows two sloped voltage regions from $\text{Li}_0\text{TiNb}_2\text{O}_7$ to $\text{Li}_{0.8}\text{TiNb}_2\text{O}_7$, and from $\text{Li}_{1.3}\text{TiNb}_2\text{O}_7$ to $\text{Li}_{3.6}\text{TiNb}_2\text{O}_7$, corresponding to the two solid solution regions respectively. A small plateau between the two sloped regions suggests a two-phase reaction region, in good agreement with the *in-situ* XRD patterns between scan 4 and scan 7. The lattice parameter refinements for a , b , c and angle β in a TiNb_2O_7 monoclinic unit cell were carried out with least square fitting for each “ x ” value in $\text{Li}_x\text{TiNb}_2\text{O}_7$; the resulting unit cell volume “ V ” and lattice parameter “ b ” are plotted in Figure 3b. It can be seen from Figure 3b that both the unit cell volume “ V ” and the lattice parameter “ b ” increase almost linearly with increasing lithium content while “ a ” and “ c ” exhibit a trendless variation (shown in Figure S8). These changes of the lattice parameters during discharge and charge are in good agreements with theoretical estimation.³⁴ The increase in b can be explained as the result of Li-ion accumulation in the (010) plane, as observed previously by spherical aberration-corrected scanning transmission electron microscopy (STEM),³⁴ i.e., with more Li ion accumulated, the coulombic repulsion between the inserted Li ions increases, leading to the expansion of the b axis. Most importantly, within experimental error, the changes of the lattice parameters and the unit-cell volume are almost completely reversible as lithium is inserted into and removed from the compound. The lattice parameters a , b and c are 20.343(4) Å, 4.111(1) Å and 11.893(4) Å, respectively, for the material after discharging to 1.0 V (corresponding to $\text{Li}_{3.6}\text{TiNb}_2\text{O}_7$). The experimental values are slightly smaller than those obtained from a first principles calculation in our previous paper, as is often the case for computations in the generalized-gradient approximation.³⁷ The unit-cell volume change for TiNb_2O_7 before and after lithium insertion (between TiNb_2O_7 and $\text{Li}_{3.6}\text{TiNb}_2\text{O}_7$) is 7.22%, much larger than that for $\text{Li}_4\text{Ti}_5\text{O}_{12}$ (less than 1% between $\text{Li}_4\text{Ti}_5\text{O}_{12}$ and $\text{Li}_7\text{Ti}_5\text{O}_{12}$). This small unit-cell volume change is considered as the main reason for the excellent cycle life for $\text{Li}_4\text{Ti}_5\text{O}_{12}$ anode material, which has been demonstrated with negligible fading after thousands of cycles in lithium-ion batteries.¹⁰ Quite interestingly, although the unit cell volume change is significantly larger than $\text{Li}_4\text{Ti}_5\text{O}_{12}$, the nanoporous TiNb_2O_7 reported here also exhibits excellent cyclic performance, mainly due to the nanoporous structure with capability to alleviate the lattice stress/strain generated from the volume expansion and contraction during lithium insertion and extraction. This stress/strain alleviation effectively ensures the structural stability of the electrode during cycling, leading to an excellent long cycle life of over 1000 cycles, comparable to that of the zero-strain anode material $\text{Li}_4\text{Ti}_5\text{O}_{12}$, but with almost twice the storage capacity.¹⁰

Ti and Nb K-edge XAS spectra were respectively collected *in situ* to examine the variations of the oxidation states of Ti and Nb. The corresponding X-ray absorption near edge spectroscopy (XANES) results are shown in Figure 3c. The Ti K-edge XANES spectrum of the pristine material shows a suppressed and split white line, indicating a distorted Ti-O octahedral environment in the crystal structure of TiNb_2O_7 . The shape of the spectra continuously changes during the discharge process, which can be attributed to the modification of the local structure by Li insertion. The sharpened white-line peak for the discharged sample (at 1.0 V, $\text{Li}_{3.6}\text{TiNb}_2\text{O}_7$) suggests a less distorted Ti-O coordination environment, well-consistent with the EXAFS results (Figure S9) and the direct observation from STEM.³⁴ Moreover, the XANES spectra demonstrate an entire edge shift, which enables us to estimate the oxidation state changes caused by Li insertion/extraction. The shift in edge energy between the pristine and lithiated TiNb_2O_7 (discharged to 1.0 V $\text{Li}_{3.6}\text{TiNb}_2\text{O}_7$) is about 3.2 eV. Under the assumption of a linear relationship³⁸ between edge shift and

oxidation state (Figure S10), these shifts correspond to an estimated change in Ti-oxidation state from Ti^{4+} in the pristine TiNb_2O_7 to $\text{Ti}^{3.2+}$ in the lithiated $\text{Li}_{3.6}\text{TiNb}_2\text{O}_7$. A similar analysis was also performed on Nb K-edge XANES spectra. An entire edge shift can be observed during Li insertion, indicating a continuous reduction of Nb. A closer inspection reveals that in the range of $0.86 \leq \text{Li} \leq 1.47$, all XANES spectra almost exactly cross at one point (shown in the inset of Figure 3c), which is called as isosbestic point^{39,40}, indicating a two-phase reaction mechanism, well-consistent with the discussion of Figure 3a for the *in situ* XRD results. Numerical values of the edge energy positions are plotted in Figure 3d. By comparing with niobium oxide standard compounds, reduction of Nb^{5+} in the pristine TiNb_2O_7 to $\text{Nb}^{3.6+}$ in the lithiated $\text{Li}_{3.6}\text{TiNb}_2\text{O}_7$ is estimated. Along with the discussion for Ti, the reductions of Ti^{4+} and Nb^{5+} are believed to start simultaneously and proceed equivalently during the initial discharge process. Oxidation states of Ti and Nb are estimated to be +3.2 and +3.6, when the electrode is fully discharged to 1.0 V. This estimate is in good agreement with the 3.6 Li inserted (estimated from the total obtained discharge capacity of 281 mAh g^{-1}), suggesting no significant side reaction (e.g. SEI formation) occurred within this voltage region (3.0 V-1.0 V). The excellent reaction reversibility is also confirmed from the observation that the Ti and Nb XANES spectra are almost shifted back completely to the pristine state (Figure S11), which is consistent with the structural reversibility revealed by *in situ* XRD and also reflected by the excellent cyclability of the nanoporous TiNb_2O_7 .

In summary, the TiNb_2O_7 with an interconnected nanoporous framework composed of nanocrystals shows a reversible storage capacity of 281 mAh g^{-1} with high coulombic efficiency at an average storage voltage of 1.66 V, which is far from the lithium plating voltage, making the battery potentially safer. Benefiting from the specific interconnected nanoporous structure, the TiNb_2O_7 anode delivers extremely high rate performance and long cycle life as demonstrated by over 1000 cycles with capacity retention of 84%. Furthermore, nanoporous TiNb_2O_7 has a high packing density, almost two times higher than that of commercial natural graphite and six times higher than that of TiO_2 nanopowder, which enables it to store more energy with the same size of the battery as with graphite or other nano-sized anode materials. When coupled with a high voltage spinel $\text{LiNi}_{0.5}\text{Mn}_{1.5}\text{O}_4$ cathode, a 3-V lithium-ion battery with excellent storage properties is further demonstrated. We believe these findings obtained here represent a significant step forward in the development of long-life, stationary lithium-ion batteries for large-scale energy storage systems.

Acknowledgements

The research at Oak Ridge National Laboratory and the University of Texas at Austin was supported by the U.S. Department of Energy’s office of Basic Energy Science, Division of Materials Sciences Engineering. The work at Brookhaven National Laboratory was supported by the U.S. Department of Energy, the Assistant Secretary for Energy Efficiency and Renewable Energy, Office of Vehicle Technologies under Contract Number DEAC02-98CH10886. The authors thank the technical supports from scientists at beamlines X14A, X18a, and X18B of National Synchrotron Light Source (NSLS). Y.S.H. thanks the funding support from NSFC (51222210) and One Hundred Talent Project of the Chinese Academy of Sciences.

Notes and references

^aChemical Sciences Division, Oak Ridge National Laboratory, Oak Ridge, Tennessee 37831 (USA). E-mail: dais@ornl.gov, guobkun@hotmail.com.

^bBrookhaven National Laboratory, Upton, New York 11973 (USA)

^cMaterials Science & Technology Division, Oak Ridge National Laboratory, Oak Ridge, Tennessee 37831 (USA)

^dBeijing National Laboratory for Condensed Matter Physics, Institute of Physics, Chinese Academy of Sciences, Beijing 100190 (China)

E-mail: yshu@aphy.iphy.ac.cn

^eDepartment of Mechanical Engineering, University of Texas at Austin, Austin, Texas 78712 (USA)

^fDepartment of Chemistry, University of Tennessee, Knoxville, Tennessee 37996 (USA)

Author contributions

B. K. G. and X. Q. Y. contribute equally to this work. S. D., B. K. G. and Y.S.H. conceived and designed this work; X. Q. Y. carried out the experiment (XRD, *in situ* XRD and XAS) and data analysis with J. L. and X.-Q. Y.; B. K. G. performed the synthesis and electrochemical performance of Ti-Nb-O electrode with X. G. S. and Z.-A. Q.; M. F. C. performed TEM observation; B. K. G., X. Q. Y., Y.S.H. and S. D. wrote the paper; J. B. G. and X.-Q. Y. edited the manuscript; all the authors participated in analysis and discussions of the results and in preparing the manuscript.

Electronic Supplementary Information (ESI) available: [details of any supplementary information available should be included here]. See DOI: 10.1039/c000000x/

- M. Armand and J. M. Tarascon, *Nature*, 2008, **451**, 652-657.
- J. B. Goodenough and Y. Kim, *Chem Mater*, 2010, **22**, 587-603.
- B. Dunn, H. Kamath and J. M. Tarascon, *Science*, 2011, **334**, 928-935.
- J. Liu, J. G. Zhang, Z. G. Yang, J. P. Lemmon, C. Imhoff, G. L. Graff, L. Y. Li, J. Z. Hu, C. M. Wang, J. Xiao, G. Xia, V. V. Viswanathan, S. Baskaran, V. Sprenkle, X. L. Li, Y. Y. Shao and B. Schwenzer, *Adv Funct Mater*, 2013, **23**, 929-946.
- M. T. McDowell, S. W. Lee, W. D. Nix and Y. Cui, *Adv Mater*, 2013, **25**, 4966-4984.
- L. M. Suo, Y.-S. Hu, H. Li, M. Armand, L. Q. Chen, *Nat Commun* 2013, **4**, 1481.
- S. Flandrois and B. Simon, *Carbon*, 1999, **37**, 165-180.
- E. Peled, C. Menachem, D. BarTow and A. Melman, *J Electrochem Soc*, 1996, **143**, L4-L7.
- D. Aurbach, B. Markovsky, I. Weissman, E. Levi and Y. Ein-Eli, *Electrochim Acta*, 1999, **45**, 67-86.
- L. Zhao, Y. S. Hu, H. Li, Z. X. Wang and L. Q. Chen, *Adv Mater*, 2011, **23**, 1385-1388.
- T. Ohzuku, A. Ueda and N. Yamamoto, *J Electrochem Soc*, 1995, **142**, 1431-1435.
- E. Ferg, R. J. Gummow, A. Dekock and M. M. Thackeray, *J Electrochem Soc*, 1994, **141**, L147-L150.
- B. K. Guo, Y. Li, Y. F. Yao, Z. Lin, L. W. Ji, G. J. Xu, Y. Z. Liang, Q. Shi and X. W. Zhang, *Solid State Ionics*, 2011, **204**, 61-65.
- E. Kang, Y. S. Jung, G. H. Kim, J. Chun, U. Wiesner, A. C. Dillon, J. K. Kim and J. Lee, *Adv Funct Mater*, 2011, **21**, 4349-4357.
- J. M. Feckl, K. Fominykh, M. Dobliger, D. Fattakhova-Rohlfing and T. Bein, *Angew Chem Int Edit*, 2012, **51**, 7459-7463.
- J. T. Han, Y. H. Huang and J. B. Goodenough, *Chem Mater*, 2011, **23**, 2027-2029.
- J. T. Han and J. B. Goodenough, *Chem Mater*, 2011, **23**, 3404-3407.
- M. D. Levi and D. Aurbach, *J Phys Chem B*, 1997, **101**, 4641-4647.
- Y. Ren, A. R. Armstrong, F. Jiao and P. G. Bruce, *J Am Chem Soc*, 2010, **132**, 996-1004.
- A. Vu, Y. Q. Qian and A. Stein, *Adv Energy Mater*, 2012, **2**, 1056-1085.
- C. K. Chan, H. L. Peng, G. Liu, K. McIlwrath, X. F. Zhang, R. A. Huggins and Y. Cui, *Nat Nanotechnol*, 2008, **3**, 31-35.
- G. Armstrong, A. R. Armstrong, P. G. Bruce, P. Reale and B. Scrosati, *Adv Mater*, 2006, **18**, 2597-+.
- J. K. Yoo, J. Kim, Y. S. Jung and K. Kang, *Adv Mater*, 2012, **24**, 5452-5456.
- K. X. Wang, M. D. Wei, M. A. Morris, H. S. Zhou and J. D. Holmes, *Adv Mater*, 2007, **19**, 3016-+.
- Y. S. Hu, L. Kienle, Y. G. Guo and J. Maier, *Adv Mater*, 2006, **18**, 1421-+.
- Y. G. Wang, Y. R. Wang, E. J. Hosono, K. X. Wang and H. S. Zhou, *Angew Chem Int Edit*, 2008, **47**, 7461-7465.
- S. T. Stern and S. E. McNeil, *Toxicol Sci*, 2008, **101**, 4-21.
- G. Oberdorster, V. Stone and K. Donaldson, *Nanotoxicology*, 2007, **1**, 2-25.
- A. Magasinski, P. Dixon, B. Hertzberg, A. Kvit, J. Ayala and G. Yushin, *Nat Mater*, 2010, **9**, 353-358.
- D. Y. Zhao, J. L. Feng, Q. S. Huo, N. Melosh, G. H. Fredrickson, B. F. Chmelka and G. D. Stucky, *Science*, 1998, **279**, 548-552.
- J. Fan, S. W. Boettcher and G. D. Stucky, *Chem Mater*, 2006, **18**, 6391-6396.
- Y. S. Hu, Y. G. Guo, W. Sigle, S. Hore, P. Balaya and J. Maier, *Nat Mater*, 2006, **5**, 713-717.
- K. Saravanan, K. Ananthanarayanan and P. Balaya, *Energy Environ Sci*, 2010, **3**, 939-948.
- X. Lu, Z. L. Jian, Z. Fang, L. Gu, Y. S. Hu, W. Chen, Z. X. Wang and L. Q. Chen, *Energ Environ Sci*, 2011, **4**, 2638-2644.
- K. Tang, X. K. Mu, P. A. van Aken, Y. Yu and J. Maier, *Adv Energy Mater*, 2013, **3**, 49-53.
- B. K. Guo, X. Q. Wang, P. F. Fulvio, M. F. Chi, S. M. Mahurin, X. G. Sun and S. Dai, *Adv Mater*, 2011, **23**, 4661-+.
- B. J. Hwang, Y. W. Tsai, D. Carlier and G. Ceder, *Chem Mater*, 2003, **15**, 3676-3682.
- X. Q. Yu, H. L. Pan, W. Wan, C. Ma, J. M. Bai, Q. P. Meng, S. N. Ehrlich, Y. S. Hu and X. Q. Yang, *Nano Lett*, 2013, **13**, 4721-4727.
- J. W. P. Moore, R. G.; Frost A. A., *John Wiley and Sons*, 1981.
- X. Q. Yu, Q. Wang, Y. N. Zhou, H. Li, X. Q. Yang, K. W. Nam, S. N. Ehrlich, S. Khalid and Y. S. Meng, *Chem Commun*, 2012, **48**, 11537-11539.